Convex Hull Based Economic Operating Region for Power Grids Considering Uncertainties of Renewable Energy Sources

Huating Xu, Bin Feng, *Student Member*, *IEEE*, Gang Huang, *Senior Member*, *IEEE*,
Mingyang Sun, *Senior Member*, *IEEE*, Houbo Xiong, *Student Member*, *IEEE*,
and Chuangxin Guo, *Senior Member*, *IEEE*

***Abstract*—The increasing integration of renewable energy sources (RESs) presents significant challenges for the safe and economical operation of power grids. Addressing the critical need to assess the effect of RES uncertainties on optimal scheduling schemes (OSSs), this paper introduces a convex hull based economic operating region (CH-EOR) for power grids. The CH-EOR is mathematically defined to delineate the impact of RES uncertainties on power grid operations. We propose a novel approach for generating the CH-EOR, enhanced by a big-*M* preprocessing method to improve the computational efficiency. Performed on four test systems, the proposed big-*M* preprocessing method demonstrates notable advancements: a reduction in average operating costs by over 10% compared with the box-constrained operating region (BC-OR) derived from robust optimization. Furthermore, the CH-EOR occupies less than 11.79% of the generators' adjustable region (GAR). Most significantly, after applying the proposed big-*M* preprocessing method, the computational efficiency is improved over 17 times compared with the traditional big-*M* method.**

***Index Terms*—Convex hull, big-*M* preprocessing method, economic operating region (EOR), renewable energy source (RES), uncertainty.**

NOMENCLATURE

A. Indices and Sets

Ψ_t	Economic operating region (EOR) at time step t
Ψ_t^{conv}	Convex hull based economic operating region (CH-EOR) at time step t
Ψ	High-dimensional EOR considering all Ψ_t
Ψ^{conv}	High-dimensional CH-EOR considering all Ψ_t^{conv}
Υ_W	Uncertainty set of active power output by renewable energy sources (RESs)
$\Omega_G, \Omega_S, \Omega_W, \Omega_D, \Omega_L$	Sets of dispatchable generators (DGs), energy storage systems (ESSs), RESs, loads, and transmission lines
Ω_T	Set of time steps from 1 to T
Ω_t^{dim}	Dimension set of CH-EOR at time step t
$\Omega_t^{lef,fac}$	Set of facets left for the next iteration at time step t
$\Omega_t^{tot,fac}$	Set of all generated facets of convex hull at time step t
$\Omega_t^{cur,fac}$	Set of current generated facets of convex hull at time step t
$\Omega_t^{tot,ver}$	Set of all generated extending points at time step t
γ	Index of dimension
i	Index of DGs
i_γ	Index of DGs corresponding to dimension γ
j	Index of RESs
l	Index of transmission lines
min, max	The minimum and maximum values
r	Index of loads
s	Index of ESSs
t	Index of time steps
V^{conv}	Set of vertices of Ψ^{conv}

B. Parameters

$\xi_{\vartheta}^{\delta,N_t^{dim}}$	N_t^{dim}-dimension vector, whose ϑ^{th} element equals δ and others are zero
$\eta_s^{cha}, \eta_s^{dis}$	Charging and discharging efficiencies of ESS s
$\pi_{l,i}^G$, $\pi_{l,j}^W$, $\pi_{l,s}^S$, $\pi_{l,r}^D$	Power transfer distribution factors associated with DG i, RES j, ESS s, and load r
a_i, b_i, c_i	Cost coefficients of DG i
c_s^{cha}, c_s^{dis}	Small positive coefficients associated with charging and discharging power of ESS s

---

Manuscript received: August 8, 2023; revised: November 28, 2023; accepted: January 22, 2024. Date of CrossCheck: January 22, 2024. Date of online publication: March 20, 2024.

This work was supported by the National Natural Science Foundation of China (No. 52007173), the National Key Research and Development Program of China (No. 2023YFB3107603), and the Science and Technology Project of State Grid Corporation (No. 5100-20212570A-0-5-SF).

H. Xu, B. Feng, G. Huang, H. Xiong, and C. Guo (corresponding author) are with the College of Electrical Engineering in Zhejiang University, Hangzhou, China (e-mail: xu_huating@zju.edu.cn; fengbinhz@zju.edu.cn; huanggang@zju.edu.cn; houboxiong@zju.edu.cn; guochuangxin@zju.edu.cn).

M. Sun is with the Department of Control Science and Engineering in Zhejiang University, Hangzhou, China (e-mail: mingyangsun@ zju.edu.cn).

DOI: 10.35833/MPCE.2023.000549

$\{cf_{\gamma,t}^{k}, df_{t}^{k}\}$	The k^{th} facet in $\Omega_t^{lef,fac}$ or $\Omega_t^{cur,fac}$, where $cf_{\gamma,t}^{k}$ is the coefficient and df_t^k is the offset
$\boldsymbol{cf}_t^k, \boldsymbol{df}_t$	Vectors consisting of $cf_{\gamma,t}^{k}$ and df_t^k, where $\boldsymbol{cf}_t^k=[cf_{\gamma,t}^{k}]$ and $\boldsymbol{df}_t=[df_t^k]$
$\boldsymbol{cf}_t$	Matrix consisting of $\boldsymbol{cf}_t^k$, $\boldsymbol{cf}_t=[\boldsymbol{cf}_t^k]$
$E_s^{\max}$	Rated capacity of ESS s
$f_l^{\max}$	The maximum transmission capacity of line l
M	A large enough constant
N_T, N_G, N_S, N_W, N_D	Numbers of scheduling time steps, DGs, ESSs, RESs, and loads
N_t^{dim}	Dimension of CH-EOR at time step t
$N_t^{lef,fac}$	Number of facets in $\Omega_t^{lef,fac}$
$p_{r,t}^D$	Active power demand of load r at time step t
$p_i^{G,\min}, p_i^{G,\max}$	The minimum and maximum active power outputs of DG i
$p_s^{S,\max}$	The maximum charging and discharging power of ESS s
RD_i, RU_i	Ramp-down and ramp-up limits of DG i
$\underline{W}_{j,t}, \overline{W}_{j,t}$	Lower and upper bounds of active power output by RES j at time step t

C. Decision Variables

$\boldsymbol{\theta}$	Vector of binary variables, $\boldsymbol{\theta}=[\theta_i]$, $\theta_i \in \{0,1\}$, $\forall i$
$\boldsymbol{\lambda}, \boldsymbol{v}$	Vectors of Lagrangian multipliers
$\boldsymbol{e}$	Vector of stored energy of ESS, $\boldsymbol{e}=[e_{s,t}]$, $\forall s, \forall t$
$\boldsymbol{p}_{cha}, \boldsymbol{p}_{dis}$	Vectors of charging and discharging power of ESS, where $\boldsymbol{p}_{cha}=[p_{s,t}^{cha}]$ and $\boldsymbol{p}_{dis}=[p_{s,t}^{dis}]$, $\forall s, \forall t$
$\boldsymbol{p}_G$	Vector of active power output by DG, $\boldsymbol{p}_G=[p_{i,t}^G]$, $\forall i, \forall t$
$\boldsymbol{p}_{G,t}^{dim}, \boldsymbol{p}_{G,t}^{0,dim}$	Vectors of $p_{i_\gamma,t}^G$ and $p_{i_\gamma,t}^{0,G}$, where $\boldsymbol{p}_{G,t}^{dim}=[p_{i_\gamma,t}^G]$, $\boldsymbol{p}_{G,t}^{0,dim}=[p_{i_\gamma,t}^{0,G}]$, $\forall i_\gamma \in \Omega_t^{dim}$
$p_{j,t}^W$	Active power output by RES j at time step t
$p_{j,t}^{W,cur}$	Curtailed power of RES j at time step t
$\boldsymbol{x}$	Vector consisting of $p_{s,t}^{cha}$, $p_{s,t}^{dis}$, $e_{s,t}$, and $p_{j,t}^{W,cur}$ i.e., $\boldsymbol{x}=[p_{s,t}^{cha}, p_{s,t}^{dis}, e_{s,t}, p_{j,t}^{W,cur}]$, $\forall s$, $\forall j$, $\forall t$

I. INTRODUCTION

THE escalating greenhouse gas emissions from fossil fuels have intensified global environmental challenges. In response, countries and regions like the European Union [1], the United States [2], and China [3] have set ambitious goals to achieve carbon neutrality by 2050, 2050, and 2060, respectively. These commitments catalyze the rapid growth of renewable energy sources (RESs). However, the inherent less predictability of RESs [4] poses risks to the operating security of power grids, and even leads to the curtailment of RESs. The effective scheduling of the dispatchable components in power grids is crucial to mitigate these risks. Current studies primarily focus on day-ahead scheduling (specific to certain RES scenarios) and security regions (often overlooking economic aspects). This paper addresses this gap by developing a convex hull based economic operating region (CH-EOR). The CH-EOR represents a global set of optimal scheduling schemes (OSSs) under RES uncertainties, aiding real-time power grid scheduling.

Worldwide scholars have employed various optimization methods to improve the power grid resilience to RES uncertainties. These methods include two-stage robust optimization [5], two-stage stochastic optimization [6], combination of robust and stochastic optimization [7], distributionally robust optimization [8], and multi-stage robust optimization [9] methods. Each method aims to optimize day-ahead scheduling for power grids integrated with RESs. Additionally, [10] and [11] explore reserve scheduling in coupled transmission and distribution grids, as well as in hybrid AC-DC grids. In [12], a local integrated electricity–heat market is designed among multiple smart energy hubs under RES uncertainties. However, the above studies predominantly concentrate on specific scenarios and do not offer comprehensive insights into the possible operating region (POR) under RES uncertainties for grid operators. This limitation has led to the advancement of region-based methods [13].

The region-based method provides global information on operating regions of power grids [14]. Reference [15] defines the security region of a distribution grid and formulates a corresponding mathematical model. Reference [16] and [17] delve into the topological characteristics and boundaries of the security regions. Reference [18] establishes a foundational theory for the security region of distribution grids, including a mathematical deduction of the $N-1$ security criterion. In [14], the focus shifts to security regions in distribution grids with soft open points. Addressing RES uncertainties, [19] introduces a set-based method to determine the maximum uncertainty boundaries for distributed generation. Reference [20] identifies the largest operating ranges of RESs, offering three alternative solving approaches. Reference [4] and [21] propose a method to construct real-time dispatchable regions for RESs, identifying them as bounded polytopes. Based on the AC power network, [22] constructs a convex inner approximation of a steady-state security region of power grid, and [23] studies the dispatchable region of RESs relative to a given dispatch base point. A novel dispatchable region considering only potential boundaries is determined through a mixed-integer linear program, as introduced in [24]. Reference [25] proposes a two-stage distributionally robust optimization model to balance system flexibility, scheduling cost, and RES utilization by co-optimizing power scheduling and operating ranges of RES. Reference [26] tackles time coupling in RESs, introducing a fast algorithm to approximate the security regions of tie-lines. Expanding this concept, [27] applies the concept of security region to multi-dimensional integrated energy systems. Reference [13] proposes a robust security region for electricity–gas integrated systems to mitigate RES fluctuations. References [28] and [29] provide a comprehensive characterization for security regions of integrated energy systems, accounting for the two-timescale feature. Additionally, [30] develops a security region based model to optimize the reactive power in distribution grids with RES uncertainties.

Regarding region utilization, [31] proposes an economic scheduling model that considers the security region of RES.

Reference [32] formulates the box-constrained operating region (BC-OR) of generators for each scheduling period, within which the real-time economic scheduling can be computed independently.

The above survey reveals significant achievements in region-based methods for various applications. However, the existing research primarily concentrates on security operating points, encompassing the security regions of distribution grids, integrated energy systems, tie-lines, AC power networks, and the dispatchable regions of RESs at specific scheduling points. To the best of the authors' knowledge, studies on the impacts of RES uncertainties on the economic operating points of power grids are relatively scarce. Different from the aforementioned studies, this paper considers both security and economics, characterizing the CH-EOR of the power grid with energy storage while taking into account the RES uncertainties.

The principal contributions of this paper are outlined as follows.

1) We define the CH-EOR of dispatchable generators (DGs) in a power grid integrated with RESs, providing the set of global OSSs under uncertainties.

2) The geometric properties of CH-EOR are delineated. Utilizing these properties, we introduce a novel approach for generating the CH-EOR. This encompasses one overarching algorithm along with two subsidiary algorithms.

3) To enhance the computational efficiency of CH-EOR, we propose a big-*M* preprocessing method.

Instead of a specific OSS, the CH-EOR, which simultaneously considers security and economics, provides a set of OSSs under uncertainties for grid operators. The CH-EOR is usually much smaller than the POR of DGs and can be calculated offline and applied online. Specifically, the applications of CH-EOR primarily include three aspects.

1) We can evaluate the economics of the real-time operation of power grid by determining whether the current operating point is within the CH-EOR [33], [34].

2) The CH-EOR can significantly reduce the action space of the artificial intelligence (AI) based algorithms for the generation of online scheduling plans and improve the training efficiency [35]-[38]. Readers can refer to [34] for details.

3) In the electricity market, CH-EOR can be regarded as a reward operating region and utilized to explore a power grid scheduling strategy that combines planned scheduling with market-based bidding [39].

The rest of this paper is organized as follows. Section II mathematically defines the CH-EOR based on a given basic optimal scheduling model (OSM) and introduces the geometric properties of CH-EOR. Section III proposes the solution approach, including a novel algorithm to calculate the CH-EOR and a big-*M* preprocessing method to accelerate the computational efficiency. Section IV presents case studies corresponding to visualization analysis, region size analysis, economy comparison, and computational efficiency comparison on four test systems. Finally, Section V gives the conclusions.

II. DEFINITION AND PROPERTIES OF CH-EOR

A. Basic OSM

The CH-EOR evaluates the optimal operating points of the dispatchable components such as DGs and energy storage systems (ESSs) in power grids and is associated with a specific OSM. The "economic" here pertains to various scheduling objectives beyond merely minimizing generation cost. In this paper, our primary focus is on the CH-EOR of DGs, with the scheduling objective set to maximize the accommodation of RESs at the lowest feasible cost. The basic OSM corresponding to this objective is formulated as:

$$\min \sum_{t=1}^{N_T}\left[\sum_{i=1}^{N_G}\left(a_i (p_{i,t}^G)^2 + b_i p_{i,t}^G + c_i\right) + \sum_{s=1}^{N_S}\left(c_s^{cha} p_{s,t}^{cha} + c_s^{dis} p_{s,t}^{dis}\right)\right] \tag{1a}$$

s.t.

$$p_i^{G,\min} \le p_{i,t}^G \le p_i^{G,\max} \quad \forall i \in \Omega_G, \forall t \in \Omega_T \tag{1b}$$

$$-RD_i \le p_{i,t+1}^G - p_{i,t}^G \le RU_i \quad \forall i \in \Omega_G, \forall t \in \Omega_{T-1} \tag{1c}$$

$$0 \le p_{j,t}^{W,cur} \le p_{j,t}^W \quad \forall j \in \Omega_W, \forall t \in \Omega_T \tag{1d}$$

$$\begin{aligned} -f_l^{\max} \le \sum_{i=1}^{N_G}\pi_{l,i}^G p_{i,t}^G + \sum_{j=1}^{N_W}\pi_{l,j}^W (p_{j,t}^W - p_{j,t}^{W,cur}) + \sum_{s=1}^{N_S}(\pi_{l,s}^{dis} p_{s,t}^{dis} - \\ \pi_{l,s}^{cha} p_{s,t}^{cha}) - \sum_{r=1}^{N_D}\pi_{l,r}^D p_{r,t}^D \le f_l^{\max} \qquad \forall l \in \Omega_L, \forall i \in \Omega_G, \\ \forall j \in \Omega_W, \forall s \in \Omega_S, \forall r \in \Omega_D, \forall t \in \Omega_T \end{aligned} \tag{1e}$$

$$e_{s,1} = e_{s,N_T+1} \quad \forall s \in \Omega_S \tag{1f}$$

$$\begin{cases} 0 \le p_{s,t}^{cha} \le p_s^{S,\max} \\ 0 \le p_{s,t}^{dis} \le p_s^{S,\max} \end{cases} \quad \forall s \in \Omega_S,\ \forall t \in \Omega_T \tag{1g}$$

$$-e_{s,t} + e_{s,t+1} + \frac{1}{\eta_s^{dis}} p_{s,t}^{dis} - \eta_s^{cha} p_{s,t}^{cha} = 0 \quad \forall s \in \Omega_S,\ \forall t \in \Omega_T \tag{1h}$$

$$\sum_{i=1}^{N_G} p_{i,t}^G + \sum_{j=1}^{N_W}(p_{j,t}^W - p_{j,t}^{W,cur}) + \sum_{s=1}^{N_S} p_{s,t}^{dis} - \sum_{s=1}^{N_S} p_{s,t}^{cha} - \sum_{r=1}^{N_D} p_{r,t}^D = 0 \quad \forall t \in \Omega_T \tag{1i}$$

Constraint (1b) restricts the output limit of DGs; constraint (1c) is the ramp limit of DGs; constraint (1d) denotes the RES curtailment; constraint (1e) limits the power flow of transmission lines; constraints (1f)-(1h) are the ESS operation conditions; and constraint (1i) is the power balance condition. Thus, the optimal solution of (1) is the OSS that corresponds to the fixed predicted value $p_{j,t}^W$.

Since (1a) is an increasing function of $p_{s,t}^{cha}$ and $p_{s,t}^{dis}$, the critical constraint $p_{s,t}^{cha} p_{s,t}^{dis} = 0$, which avoids simultaneous charging and discharging, is always satisfied at the optimal solution [40]. Please refer to [40] for details of the proof.

It is worth mentioning that the basic OSM (1) is constructed based on the DC power flow model, which is widely accepted in economic scheduling problems, and the modeling error meets engineering needs [41]. The CH-EOR based on the AC power flow model is our future research.

B. Definition of CH-EOR

In this subsection, we mathematically define the CH-EOR corresponding to the basic OSM (1) as follows.

Definition 1 Let $\varPsi_t = \{\boldsymbol{p}_{G,t} | \forall \boldsymbol{p}_W \in \varUpsilon_W,\ \exists p_{G,t} \text{ satisfies (1)}\}$, and then the CH-EOR at time step t, denoted as $\varPsi_t^{conv}$, is $conv(\varPsi_t)$, and $\boldsymbol{p}_{G,t} = [p_{i,t}^G], \forall i$.

According to Definition 1, $\varPsi_t$ is the set of OSSs of DGs at time step t, which is the exact economic operating region (EOR). Since the mapping from $\boldsymbol{p}_W$ to $\boldsymbol{p}_{G,t}$ is non-linear, whether $\varUpsilon_W$ is convex or not, $\varPsi_t$ may be a non-convex set which is notoriously hard to handle. To balance the utility and complexity, we calculate the convex hull of $\varPsi_t$, i.e., the so-called CH-EOR $\varPsi_t^{conv}$. In the following, $\varPsi_t^{conv}$ corresponds specifically to the DGs in the basic OSM (1) unless stated otherwise.

Figure 1 presents a schematic diagram showing the difference and relationship among generators' adjustable region (GAR), POR, EOR, and CH-EOR in 2D space. GAR is the set of all possible combined outputs of DGs that only considers output limits of DGs. POR is the set of all possible operating points that only satisfy security constraints (1b)-(1i) (usually the subset of GAR). CH-EOR is the convex hull of EOR, usually much smaller than POR and GAR. POR only considers "feasible and robust" aspects, while EOR and CH-EOR, in addition to this, also take into account system economics.

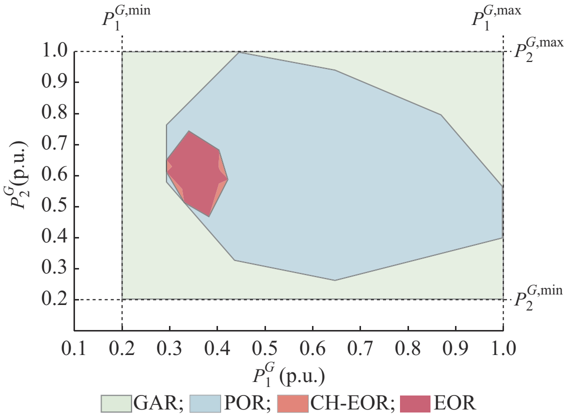

Fig. 1. Schematic diagram of GAR, POR, EOR, and CH-EOR.

C. Properties of CH-EOR

In order to develop a computational algorithm for CH-EOR, we first derive its geometric property. For the convenience of expression, the basic OSM (1) is written in a compact form as:

$$\min\,(\boldsymbol{p}_G^{\mathrm{T}}\boldsymbol{A}\boldsymbol{p}_G + \boldsymbol{B}^{\mathrm{T}}\boldsymbol{p}_G + \boldsymbol{C}^{\mathrm{T}}\boldsymbol{x} + \boldsymbol{D}) \tag{2a}$$

s.t.

$$\boldsymbol{E}_1\boldsymbol{p}_G + \boldsymbol{F}_1\boldsymbol{p}_W + \boldsymbol{G}_1\boldsymbol{x} + \boldsymbol{H}_1 \le \boldsymbol{0} \tag{2b}$$

$$\boldsymbol{E}_2\boldsymbol{p}_G + \boldsymbol{F}_2\boldsymbol{p}_W + \boldsymbol{G}_2\boldsymbol{x} + \boldsymbol{H}_2 = \boldsymbol{0} \tag{2c}$$

where matrices $\boldsymbol{A}, \boldsymbol{E}_1, \boldsymbol{E}_2, \boldsymbol{F}_1, \boldsymbol{F}_2, \boldsymbol{G}_1$, and $\boldsymbol{G}_2$, vectors $\boldsymbol{B}$, $\boldsymbol{C}$, $\boldsymbol{H}_1$, and $\boldsymbol{H}_2$, and constant $\boldsymbol{D}$ correspond to the coefficients in (1).

Since (2) is a quadratic convex optimization problem, the Karush-Kuhn-Tucker (KKT) conditions are both necessary and sufficient for its optimal solution [42] and can be formulated as:

$$\begin{cases} \text{(2b)} \\ \text{(2c)} \\ \boldsymbol{\lambda} \ge \boldsymbol{0} \end{cases} \tag{3a}$$

$$\mathrm{diag}(\boldsymbol{\lambda})\cdot(\boldsymbol{E}_1\boldsymbol{p}_G + \boldsymbol{F}_1\boldsymbol{p}_W + \boldsymbol{G}_1\boldsymbol{x} + \boldsymbol{H}_1) = \boldsymbol{0} \tag{3b}$$

$$2\boldsymbol{A}\boldsymbol{p}_G + \boldsymbol{B} + \boldsymbol{E}_1^{\mathrm{T}}\boldsymbol{\lambda} + \boldsymbol{E}_2^{\mathrm{T}}\boldsymbol{v} = \boldsymbol{0} \tag{3c}$$

$$\boldsymbol{C} + \boldsymbol{G}_1^{\mathrm{T}}\boldsymbol{\lambda} + \boldsymbol{G}_2^{\mathrm{T}}\boldsymbol{v} = \boldsymbol{0} \tag{3d}$$

Constraint (3b) consists of q_1 rows, which is the dimension of $\boldsymbol{\lambda}$.

Proposition 1 If the uncertainty set $\varUpsilon_W$ is a bounded polytope, so is $\varPsi_t^{conv}, \forall t \in \varOmega_T$.

Proof See Appendix A.

Proposition 1 reveals that $\varPsi_t^{conv}$ can be formulated by linear inequalities as:

$$\varPsi_t^{conv} = \{\boldsymbol{p}_{G,t}^{dim} | \boldsymbol{cf}_t \cdot \boldsymbol{p}_{G,t}^{dim} + \boldsymbol{df}_t \le \boldsymbol{0}\} \tag{4}$$

Thus, our remaining work is to determine the dimension of CH-EOR N_t^{dim}, the matrix $\boldsymbol{cf}_t$, and the vector $\boldsymbol{df}_t$, $\forall t \in \varOmega_T$. Some additional remarks about the CH-EOR are given as follows.

1) Since the main contribution of this paper is not the characterization of uncertainty sets, we have only chosen to use box constraints for simplicity to represent the uncertainty set $\varUpsilon_W$ of RESs (a common practice in robust optimization [10]). The uncertainty set can also be modified to other convex forms [43] by replacing the corresponding constraints, and the resulting compact form will remain unchanged with the same solution process. The acceleration strategy introduced in Section III also works.

2) The attributes of CH-EOR including time scale, temporal resolution, basic OSM, etc. are tailored to meet specific scheduling requirements. Additionally, the unit commitment can be integrated into the basic OSM, which is the future research.

3) The dimension of $\varPsi_t^{conv}$, denoted as N_t^{dim}, corresponds to the number of DGs whose optimal output is influenced by RESs. It is important to note that N_t^{dim} may be smaller than the total number of DGs because certain DGs may maintain a constant optimal output regardless of the fluctuations of RESs within the uncertainty set. As demonstrated in Section IV, $\varPsi_t^{conv}$ is considerably smaller than the POR of DGs. We can develop efficient algorithms to match the OSS from the CH-EOR for real-time scheduling.

III. SOLUTION APPROACH

A. Overall Algorithm

This subsection presents the overall algorithm (Algorithm 1) for CH-EOR calculation. The main idea is first to determine the dimension of $\varPsi_t^{conv}$ and initialize a convex hull with the same dimension for each time step, ensuring it is sufficiently small. Subsequently, extending points are computed, and the initial convex hulls are iteratively expanded. The overall calculation process of the overall algorithm is illustrated in Fig. 2.

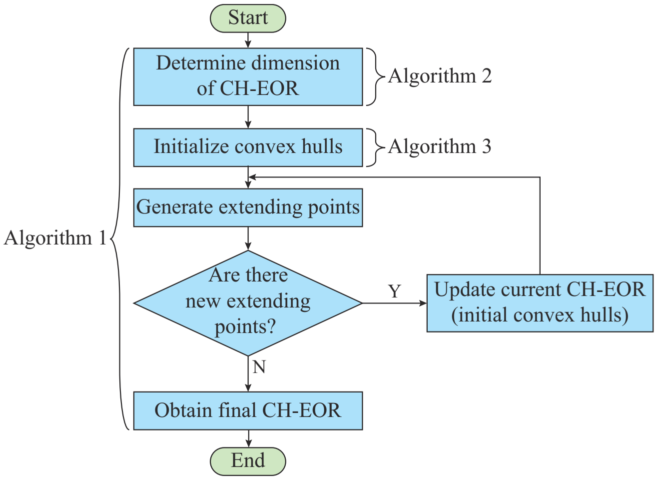

Fig. 2. Overall calculation process of overall algorithm.

Since Proposition 1 reveals that the CH-EOR is a bounded polytope, the final CH-EOR can be obtained within a finite number of iterations. The detailed calculation process of CH-EOR is outlined in Algorithm 1. The CH-EOR Ψ_t^{conv} is iteratively calculated until $\Omega_t^{lef,fac}$ is empty for all time steps (the outer loop starting from line 5). Extending points of Ψ_t^{conv} are independently generated for each time step (the middle loop starting from line 6) and each facet (the inner loop starting from line 7).

```
Algorithm 1: calculation process of CH-EOR
Input: $N_T$ and tolerance $\delta_1$
Output: the facets $\{cf_{\gamma,t}^k, df_t^k\} \in \Omega_t^{cur,fac}$, $\forall \gamma, \forall k, \forall t$
1: Initialize $\Omega_t^{tot,fac} = \varnothing$, $\Omega_t^{cur,fac} = \varnothing$, $\Omega_t^{lef,fac} = \varnothing$, and $\Omega_t^{tot,ver} = \varnothing$
2: Determine the dimension of CH-EOR for each time step, and obtain
     $\Omega_t^{dim}$, $N_t^{dim}$, $\forall t \in \Omega_T$ (Algorithm 2)
3: Initialize sufficiently small convex hulls for each time step, and update
     $\Omega_t^{tot,ver}$ and $\Omega_t^{cur,fac}$, $\forall t \in \Omega_T$ (Algorithm 3)
4: Update $\Omega_t^{lef,fac} = \Omega_t^{cur,fac}$, $\forall t \in \Omega_T$
5: While $\exists t \in \Omega_T$, $\Omega_t^{lef,fac} \neq \varnothing$, do
6:   for $t = 1{:}N_T$ do
7:     for $k = 1{:}N_t^{lef,fac}$ do
8:       Solve the optimization problem based on $\{cf_{\gamma,t}^k, df_t^k\} \in \Omega_t^{lef,fac}$ to obtain
           an potential extending point $\boldsymbol{p}_{G,t}^{dim}$ and calculate
           $d = \left|\sum_{\gamma} cf_{\gamma,t}^k \cdot p_{i_\gamma,t}^G + df_t^k\right| \Big/ \sqrt{\sum_{\gamma} (cf_{\gamma,t}^k)^2}$
9:       if $d > \delta_1$ then
10:        Update $\Omega_t^{tot,ver} = \Omega_t^{tot,ver} \cup \{\boldsymbol{p}_{G,t}^{\dim}\}$
11:      end
12:  end
13:  Calculate the half-space representation of the convex hull of vertices
       in $\Omega_t^{tot,ver}$ based on the quickhull algorithm [44], update $\Omega_t^{cur,fac}$ with
       all the obtained facets, update $\Omega_t^{lef,fac} = \Omega_t^{cur,fac} \setminus \Omega_t^{tot,fac}$, and update
       $\Omega_t^{tot,fac} = \Omega_t^{tot,fac} \cup \Omega_t^{cur,fac}$
14:  end
15: end
```

1) Determining Dimensions

To identify the DGs whose outputs remain unchanged with the RESs and ascertain the dimension of CH-EOR, we present two distinct bi-level optimization problems, denoted as (5) and (6), and each is solvable independently for every $p_{i,t}^G$.

$$\max p_{i,t}^G \tag{5a}$$

s.t.

$$\underline{W}_{j,t} \leq p_{j,t}^W \leq \overline{W}_{j,t} \quad \forall j \in \Omega_W, \forall t \in \Omega_T \tag{5b}$$

$$[\boldsymbol{p}_G, \boldsymbol{x}] \in \arg\{\min(2a), \text{s.t.}\ (2b), (2c)\} \tag{5c}$$

$$\min p_{i,t}^G \tag{6a}$$

s.t.

$$\underline{W}_{j,t} \leq p_{j,t}^W \leq \overline{W}_{j,t} \quad \forall j \in \Omega_W, \forall t \in \Omega_T \tag{6b}$$

$$[\boldsymbol{p}_G, \boldsymbol{x}] \in \arg\{\min(2a), \text{s.t.}\ (2b), (2c)\} \tag{6c}$$

As shown in (5b) and (6b), we assume that $p_{j,t}^W$ lies within the lower and upper bounds of the active power output by RES. Constraints (5c) and (6c) involve lower-level optimizations guaranteeing that $[\boldsymbol{p}_G, \boldsymbol{x}]$ satisfies the basic OSM (2), ensuring optimality. Consequently, constraints (5b) ((6b)) and (5c) ((6c)) define the set Ψ_t, and objectives (5a) and (6a) seek the maximum value $p_{i,t}^{opt,\max}$ and the minimum value $p_{i,t}^{opt,\min}$ of $p_{i,t}^G$ in Ψ_t, respectively, with the output power fluctuation of RES within the uncertain set. If $p_{i,t}^{opt,\max} = p_{i,t}^{opt,\min}$, which indicates a fixed optimal $p_{i,t}^G$, the corresponding DG can be removed. However, it is not straightforward for off-the-shelf solvers to solve bi-level optimization problems. To address this, we propose replacing the lower-level optimization problem with its KKT conditions (3a)-(3d) [42]. Since it is challenging due to the non-convex complementary slackness condition (3b), we employ the following linearization technique [4] to reformulate (3b).

$$-M\boldsymbol{\theta} \leq \boldsymbol{E}_1 \boldsymbol{p}_G + \boldsymbol{F}_1 \boldsymbol{p}_W + \boldsymbol{G}_1 \boldsymbol{x} + \boldsymbol{H}_1 \leq \boldsymbol{0} \tag{7a}$$

$$\boldsymbol{0} \leq \boldsymbol{\lambda} \leq M(\boldsymbol{1} - \boldsymbol{\theta}) \tag{7b}$$

Thus, the bi-level optimization problems (5) and (6) are reformulated as the single-level problems (8) and (9), respectively, which can be solved by commercial solvers directly.

$$\begin{cases} \max p_{i,t}^G \\ \text{s.t.}\ (3a), (3c), (3d), (5b), (7a), (7b) \end{cases} \tag{8}$$

$$\begin{cases} \min p_{i,t}^G \\ \text{s.t.}\ (3a), (3c), (3d), (5b), (7a), (7b) \end{cases} \tag{9}$$

Taking into account calculation errors, the procedure for determining the dimension of CH-EOR is outlined in Algorithm 2.

```
Algorithm 2: determining the dimension of CH-EOR
Input: $N_T$ and tolerance $\delta_2$
Output: $N_t^{dim}$ and $\Omega_t^{dim}$, $\forall t \in \Omega_T$
Initialize $N_t^{dim} = 0$ and $\Omega_t^{dim} = \varnothing$, $\forall t \in \Omega_T$
for $t = 1{:}N_T$ do
  for $i = 1{:}N_G$ do
    Solve (8) and (9) to obtain $p_{i,t}^{opt,\max}$ and $p_{i,t}^{opt,\min}$
    if $\left|p_{i,t}^{opt,\max} - p_{i,t}^{opt,\min}\right| \geq \delta_2$ then
      Update $\Omega_t^{dim} = \Omega_t^{dim} \cup \{i\}$, $N_t^{dim} = N_t^{dim} + 1$
    end
  end
end
```

2) Initializing Convex Hulls

In this part, we initiate the iterative calculation of CH-EOR by formulating small simplexes as the initial convex hulls. Initially, a scenario is randomly chosen from the uncertainty set of RES outputs, and the basic OSM (1) is solved to obtain a specific OSS, denoted as $\{p_{i,t}^{0,G}\}, \forall i, \forall t$. Subsequently, for each time step, N_t^{dim} points are generated by introducing slight deviations to each dimension of the optimal solution. These points, along with the optimal solution, constitute $N_t^{dim}+1$ vertices in $\Omega_t^{tot,ver}$. The next step involves computing the half-space representation of the simplex using the quickhull algorithm [44]. The obtained facets are used to update $\Omega_t^{cur,fac}$. Algorithm 3 provides a detailed description of this calculation process.

Algorithm 3: initializing convex hulls

```
Input: $N_T$, $N_t^{dim}$, $\Omega_t^{dim}$, $\forall t \in \Omega_T$, and deviation $\delta$
Output: $\Omega_t^{tot,ver}$ and $\Omega_t^{cur,fac}$, $\forall t \in \Omega_T$
1: Initialize $\Omega_t^{tot,ver} = \varnothing$ and $\Omega_t^{cur,fac} = \varnothing$
2: Solve the basic OSM (1) to obtain the optimal solution $\{p_{i,t}^{0,G}\}, \forall i, \forall t$
       based on a specific RES output scenario
3: for $t = 1{:}N_T$ do
4:     Update $\Omega_t^{tot,ver} = \Omega_t^{tot,ver} \cup \boldsymbol{p}_{G,t}^{0,dim}$
5:     for $\vartheta = 1{:}N_t^{dim}$ do
6:         Update $\Omega_t^{tot,ver} = \Omega_t^{tot,ver} \cup \left\{\boldsymbol{p}_{G,t}^{0,dim} + \boldsymbol{\xi}_{\vartheta}^{\delta, N_t^{dim}}\right\}$
7:     end
8:     Calculate the half-space representation $\{cf_{\gamma,t}^k, df_t^k\}$ of the convex hull
           of the vertices in $\Omega_t^{tot,ver}$ based on the quickhull algorithm [44]
9:     Update $\Omega_t^{cur,fac} = \Omega_t^{cur,fac} \cup \{cf_{\gamma,t}^k, df_t^k\}, \forall k$
10: end
```

3) Searching Extending Points

According to Algorithm 3, the CH-EOR is systematically expanded through the iterative search for extending points beyond the current convex hull. We formulate the bi-level optimization problem (10) to generate these extending points. Constraints (10b) and (10c) confine $p_{i,t}^G$ within the set Ψ_t, which is the same as 5(b)(6(b)) and 5(c)(6(c)), respectively. The objective function (10a) is designed to identify the farthest point $p_{G,t}^{dim}$ above the facet $\{cf_{\gamma,t}^k, df_t^k\}$.

$$\max \sum_{\gamma=1}^{N_t^{dim}} cf_{\gamma,t}^k \cdot p_{i_\gamma,t}^G + df_t^k \quad i_\gamma \in \Omega_t^{dim} \tag{10a}$$

s.t.

$$\underline{W}_{j,t} \le p_{j,t}^W \le \overline{W}_{j,t} \quad \forall j \in \Omega_W, \forall t \in \Omega_T \tag{10b}$$

$$[\boldsymbol{p}_G, \boldsymbol{x}] \in \arg\{\min(2\text{a}), \text{ s.t. } (2\text{b}), (2\text{c})\} \tag{10c}$$

As introduced in Section III-A-1), the bi-level optimization problem (10) can also be transformed into a single-level form, obtaining the mixed-integer linear programming problem (11).

$$\max \sum_{\gamma=1}^{N_t^{dim}} cf_{\gamma,t}^k \cdot p_{i_\gamma,t}^G + df_t^k \quad i_\gamma \in \Omega_t^{dim} \tag{11a}$$

s.t.

$$(3\text{a}), (3\text{c}), (3\text{d}), (5\text{b}), (7\text{a}), (7\text{b}) \tag{11b}$$

Proposition 2 If the vector $\boldsymbol{cf}_t^k$ is not orthogonal to any facet of CH-EOR Ψ_t^{conv}, then the extending point generated based on $\{cf_{\gamma,t}^k, df_t^k\}$ is the extreme point of Ψ_t^{conv}.

Proof See Appendix A.

According to Proposition 1, Proposition 2, and Algorithm 1, we can deduce that after a finite number of iterations, the iterative process will converge to the final CH-EOR. Though the CH-EORs are generated for each period, they are closely connected through ramping and energy storage constraints. In our bi-level optimization problem (10) for generating CH-EOR vertices, the lower-level optimization (10c) considers the ramping and energy storage constraints between all scheduling periods.

B. Acceleration Strategy

In Section III-A-1), constraint (3b) undergoes linearization using the big-M method. However, the traditional big-M method employs a uniform value of M for every constraint, posing challenges in determining an appropriate value and leading to overly relaxed node bounds. This results in a higher number of nodes requiring examination during the branching process. To address this limitation, we propose a big-M preprocessing method to tailor a specific M for each respective constraint, tightening the node relaxation and subsequently improving the efficiency of the solution process.

Firstly, randomly generate N_{sce} scenarios for RES output, denoted as $\boldsymbol{p}_W^n$ $(n = 1, 2, ..., N_{sce})$, based on which the basic OSM (2) is solved to obtain the corresponding optimal solutions $[\boldsymbol{p}_G^n, \boldsymbol{x}^n]$ $(n = 1, 2, ..., N_{sce})$. Then, solve the following linear optimization problem (12) for each scenario to obtain $\boldsymbol{\lambda}^n$ and $\boldsymbol{v}^n$ $(n = 1, 2, ..., N_{sce})$.

$$\min \boldsymbol{1}^{\mathrm{T}} \boldsymbol{\lambda}^n \tag{12a}$$

s.t.

$$\begin{cases} \lambda_i^n = 0 \\ \boldsymbol{E}_{1i}\boldsymbol{p}_G^n + \boldsymbol{F}_{1i}\boldsymbol{p}_W^n + \boldsymbol{G}_{1i}\boldsymbol{x}^n + \boldsymbol{H}_{1i} \ne \boldsymbol{0} \end{cases} \quad \forall i \tag{12b}$$

$$\begin{cases} \lambda_i^n \ge 0 \\ \boldsymbol{E}_{1i}\boldsymbol{p}_G^n + \boldsymbol{F}_{1i}\boldsymbol{p}_W^n + \boldsymbol{G}_{1i}\boldsymbol{x}^n + \boldsymbol{H}_{1i} = \boldsymbol{0} \end{cases} \quad \forall i \tag{12c}$$

$$2\boldsymbol{A}\boldsymbol{p}_G^n + \boldsymbol{B} + \boldsymbol{E}_1^{\mathrm{T}}\boldsymbol{\lambda}^n + \boldsymbol{E}_2^{\mathrm{T}}\boldsymbol{v}^n = \boldsymbol{0} \tag{12d}$$

$$\boldsymbol{C} + \boldsymbol{G}_1^{\mathrm{T}}\boldsymbol{\lambda}^n + \boldsymbol{G}_2^{\mathrm{T}}\boldsymbol{v}^n = \boldsymbol{0} \tag{12e}$$

where $\boldsymbol{E}_{1i}$, $\boldsymbol{F}_{1i}$, $\boldsymbol{G}_{1i}$, and $\boldsymbol{H}_{1i}$ are the i^{th} row of $\boldsymbol{E}_1$, $\boldsymbol{F}_1$, $\boldsymbol{G}_1$ and $\boldsymbol{H}_1$, respectively; and λ_i^n and v_i^n are the i^{th} element of $\boldsymbol{\lambda}^n$ and $\boldsymbol{v}^n$, respectively. Since $[\boldsymbol{p}_G^n, \boldsymbol{x}^n]$ is solved ahead of time, it is easy to identify the non-active inequality constraints and restrict the corresponding λ_i^n to zero (constraint (12b)). Similarly, constraint (12c) determines the ranges of λ_i^n related to the active inequalities. Constraints (12b) and (12c) are equivalent to complementary slackness conditions and dual feasibility. Constraints (12d) and (12e) are stationary conditions. Since $[\boldsymbol{p}_G^n, \boldsymbol{x}^n]$ is the optimal solution of the basic OSM (2) based on $\boldsymbol{p}_W^n$, the primal feasibility is inherently satisfied. Thus, the obtained $\boldsymbol{\lambda}^n$ and $\boldsymbol{v}^n$ satisfy the KKT conditions (3).

After that, we replace M corresponding to $\boldsymbol{\lambda}_i$ in (7) with $M_i^{\boldsymbol{\lambda},\max}$ and bound $\boldsymbol{v}_i$ in (13) with $M_i^{\boldsymbol{v},\max}$ and $M_i^{\boldsymbol{v},\min}$. $M_i^{\boldsymbol{\lambda},\max}$, $M_i^{\boldsymbol{v},\max}$, and $M_i^{\boldsymbol{v},\min}$ are calculated as:

$$M_i^{\boldsymbol{\lambda},\max} = \min\{\lambda_i^{\max} m_1 + m_2, \ m_3\} \tag{13a}$$

$$M_i^{\boldsymbol{v},\max} = \min\{v_i^{\max} + \left|v_i^{\max}\right| m_1 + m_2, \ m_3\} \tag{13b}$$

$$M_i^{\boldsymbol{v},\min} = \max\{v_i^{\min} - \left|v_i^{\min}\right| m_1 - m_2, \ -m_3\} \tag{13c}$$

where $\lambda_i^{\max} = \max\{\lambda_i^n \left| \boldsymbol{E}_{1i}\boldsymbol{p}_G^n + \boldsymbol{F}_{1i}\boldsymbol{p}_W^n + \boldsymbol{G}_{1i}\boldsymbol{x}^n + \boldsymbol{H}_{1i} \right|\}, \forall n$; $v_i^{\max} = \max\{v_i^n\}, \forall n$; $v_i^{\min} = \min\{v_i^n\}, \forall n$; and m_1, m_2, and m_3 are the given positive constants that are easy to determine. We obtain $M_i^{\boldsymbol{\lambda},\max}$, $M_i^{\boldsymbol{v},\max}$, and $M_i^{\boldsymbol{v},\min}$ by solving linear optimization problems, which usually take much less time than solving mix-integer problems.

As detailed in Section III-A, the computation of CH-EOR involves the iterative solution of the mix-integer optimization problems. The proposed big-M preprocessing method tightens the node relaxation during the branching process and plays a crucial role in enhancing computational efficiency (substantiated in Section IV-D).

IV. CASE STUDIES

This section presents case studies conducted on modified IEEE 9-bus, IEEE 30-bus, IEEE 57-bus, and IEEE 118-bus test systems [45]. All experiments are performed on a computer with a 2.90 GHz CPU and 16 GB RAM. Gurobi 9.5.1 is utilized under a Free Academic License.

A. General Experimental Setup

To investigate the characteristics of CH-EOR and validate the effectiveness of Algorithm 1, we modify four test systems by incorporating two wind farms (RES 1 and RES 2) and one energy storage system (ESS), to which the corresponding buses are detailed in Table I. Additionally, Table II provides the operation parameters for DGs and ESSs, including the ramp-up/ramp-down limits for DGs and the rated capacity, the maximum charging/discharging power, and charging/discharging efficiency for ESSs. The initial stored electrical energy for each ESS is set to half its capacity.

TABLE I
BUS NO. CORRESPONGDING TO FOUR TEST SYSTEMS

Test system	Bus No.			
	RES 1	RES 2	ESS	DGs
IEEE 9-bus	7	9	5	1, 2, 3
IEEE 30-bus	6	12	12	1, 2, 22, 27
IEEE 57-bus	8	12	9	1, 3, 8, 12
IEEE 118-bus	12	49	9	5, 11, 12, 21, 28, 29, 30, 37, 40, 45

TABLE II
OPERATION PARAMETERS OF DGS AND ESSS

Test system	RD_i (MW/h)	RU_i (MW/h)	$E_1^{\max}$ (MWh)	$p_1^{S,\max}$ (MW)	η_s^{cha}	η_s^{dis}
IEEE 9-bus	30	30	200	25	0.93	0.93
IEEE 30-bus	30	30	200	25	0.93	0.93
IEEE 57-bus	100	100	500	100	0.93	0.93
IEEE 118-bus	200	200	500	100	0.93	0.93

To facilitate experimental design, we set $N_T = 24$ and assume that the predicted output power of RESs and the load level for each test system fluctuate based on the factors outlined in Appendix A. At each time step, the predicted output power of RES is determined by multiplying a base power by the corresponding RES factor, and the load is calculated by multiplying a base load by the corresponding load factor. The base power of RES is set to be 30 MW, 40 MW, 100 MW, and 200 MW for the IEEE 9-bus, IEEE 30-bus, IEEE 57-bus, and IEEE 118-bus test systems, respectively. The base loads are given in the IEEE 30-bus, IEEE 57-bus, and IEEE 118-bus test systems, where they are adjusted to 80 MW, 60 MW, and 60 MW, connected to buses 5, 7, and 9, respectively. In the IEEE 9-bus, IEEE 30-bus, and IEEE 57-bus test systems, the minimum output power of each DG is set to be 30% of its rated power.

More specifically, in the IEEE 9-bus test system, the rated output power of each DG is set to be 100 MW and the branch transmission limit is shown in Table III. In the IEEE 30-bus test system, we adjust the branch transmission limit to twice the specified value. In the IEEE 57-bus test system, each branch transmission limit is set to be 200 MW. In the IEEE 118-bus test system, each branch transmission limit is set to be 300 MW. Other parameters are configured as: $c_s^{cha} = c_s^{dis} = 0.01$, $\delta_1 = 0.1$, $\delta_2 = 0.02$, and $N_{sce} = 500$.

TABLE III
BRANCH TRANSMISSION LIMIT IN IEEE 9-BUS TEST SYSTEM

Branch No.	Connected bus	Transmission limit (MVA)
1	(1, 4)	170
2	(4, 5)	80
3	(5, 6)	70
4	(3, 6)	170
5	(6, 7)	70
6	(7, 8)	170
7	(8, 2)	170
8	(8, 9)	100
9	(9, 4)	70

B. Visualization and Region Size Analysis

To gain a more intuitive understanding of CH-EOR, we apply the proposed big-M preprocessing method to the IEEE 9-bus test system, which features three DGs and is particularly suitable for the visualization analysis of CH-EOR. We assume that the actual output power of wind farms falls within ±65% of the predicted value, constituting the uncertainty set Υ_W. The CH-EOR is calculated for scenarios without ESS in operation (denoted as CH-EOR 1) and with ESS in operation (denoted as CH-EOR 2). Additionally, we introduce the POR of DG for comparison, which solely considers security constraints and disregards the ESS and optimality condition. Calculations are performed for CH-EOR 1, CH-EOR 2, and POR across 24 time steps. For a detailed analysis, we select time steps 1, 2, 5, and 20 for visualization, as illustrated in Fig. 3.

While the IEEE 9-bus test system incorporates three DGs, it is noteworthy that the dimensions of CH-EOR at each time step are not consistently three, indicating dimension reduction. As illustrated in Fig. 3 and detailed in Table IV, the dimensions of CH-EOR 1 decrease to 2 at time steps 2, 4, 6, and 24. Similarly, the dimensions of CH-EOR 2 decrease to 2 at time steps 1-9. In contrast, the dimensions of POR remain constant at 3. The phenomenon of dimension reduction in CH-EOR implies that, at certain time steps, the optimal output power of the corresponding DGs (DG 1 in this case study) remains fixed at 30 MW, regardless of fluctuations in the wind farms within the uncertainty set. This stability in the optimal output power of DGs can be utilized to guide real-time scheduling.

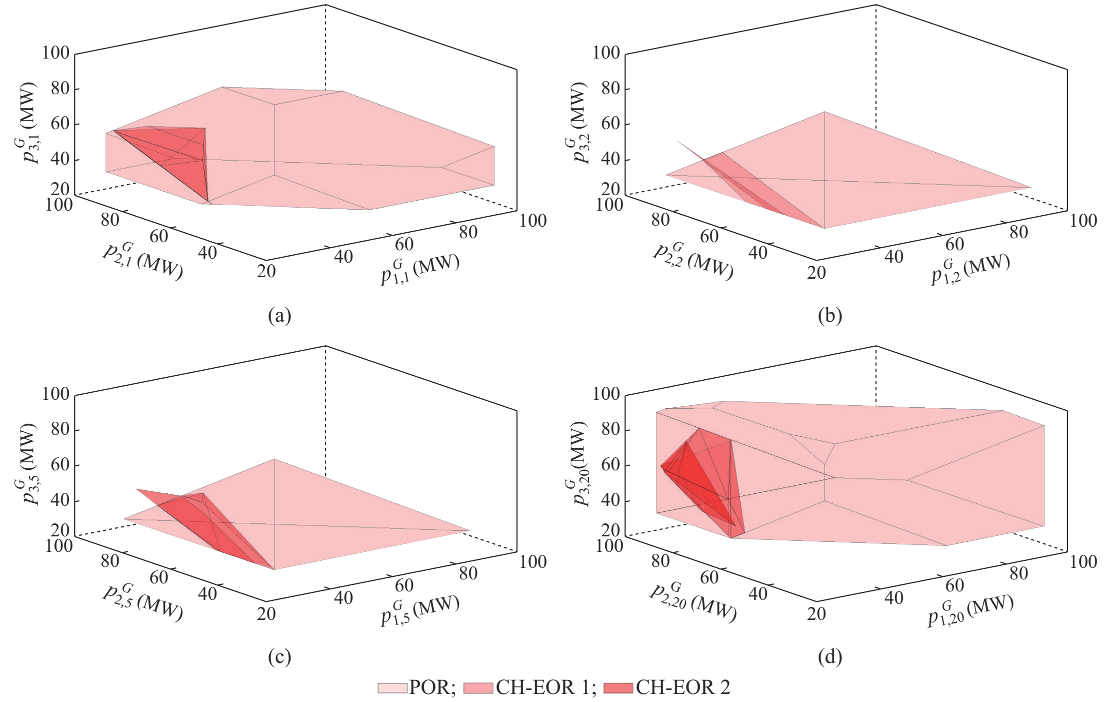

(a)
(b)
(c)
(d)

Fig. 3. Visualization of CH-EOR 1, CH-EOR 2, and POR. (a) Time step 1. (b) Time step 2. (c) Time step 5. (d) Time step 20.

TABLE IV
Region Size and Dimendions of POR, CH-EOR 1, and CH-EOR 2

Time step	POR		CH-EOR 1		CH-EOR 2	
	Ratio (%)	Dimension	Ratio (%)	Dimension	Ratio (%)	Dimension
1	34.74	3	0.72	3	0.18	2
2	14.06	3	10.59	2	1.63	2
3	13.73	3	0.18	3	1.17	2
4	10.63	3	10.92	2	0.27	2
5	11.98	3	0.14	3	9.87	2
6	9.83	3	11.79	2	5.10	2
7	14.04	3	0.29	3	9.15	2
8	12.70	3	0.23	3	11.57	2
9	12.73	3	0.25	3	6.10	2
10	23.76	3	1.07	3	0.39	3
11	42.96	3	1.96	3	0.49	3
12	69.52	3	3.27	3	0.78	3
13	67.63	3	1.20	3	0.04	3
14	67.59	3	0.47	3	0.02	3
15	52.76	3	0.14	3	0.02	3
16	57.22	3	0.21	3	0.02	3
17	56.55	3	0.19	3	0.02	3
18	73.21	3	0.70	3	0.03	3
19	75.03	3	1.78	3	0.18	3
20	69.52	3	1.38	3	0.28	3
21	68.08	3	0.29	3	0.24	3
22	60.98	3	2.09	3	1.50	3
23	13.15	3	0.18	3	0.30	3
24	13.73	3	5.47	2	0.29	3

The primary distinction between the POR and CH-EOR 1 lies in the additional consideration of the optimality condition in CH-EOR 1. Consequently, CH-EOR 1 remains within the bounds of POR. However, when the ESS is in operation, the corresponding CH-EOR 2 exceeds the limits of POR at certain time steps due to the ability of ESS to transfer electrical energy and alter the optimal operating region of DG. As illustrated in Fig. 3, it is evident that the POR constitutes a substantial portion of GAR. Nevertheless, after factoring in the optimality condition, the CH-EOR becomes relatively small, restricting the output power of DG 1 to a lower level (attributed to the high generation cost of DG 1). At time step 1, CH-EOR 2 even contracts into a very narrow region.

Furthermore, we assess the region size of POR, CH-EOR 1, and CH-EOR 2 using the Monte Carlo method, with the corresponding ratios to the GAR, as presented in Table IV. Based on the RES factors in Appendix A and a given RES forecast error of ±65%, the uncertain RES output constitutes 7.45%-77.545% of the load and 5.13%-44.17% of installed capacity of DGs. In a context characterized by significant RES uncertainty, the POR spans from 9.83% to 75.03%. However, CH-EOR 1 encompasses only 0.14%-3.27% in three dimensions and 5.47%-11.79% in two dimensions. CH-EOR 2 covers 0.02%-1.50% in three dimensions and 0.18%-11.57% in two dimensions.

Based on the preceding discussions, it is observed that the EOR of DGs typically constitutes a minor ratio of their GAR, which is also considerably smaller than the POR. The proposed big-M processing method effectively delineates this EOR. The inclusion of ESS serves to further contract the CH-EOR, even reducing its dimensionality. This contraction concentrates the operating points of DGs within a more economically favorable region.

C. Economic Comparison

This subsection examines the economic characteristics of CH-EOR and compares them with the box-constrained operating region (BC-OR) [32], utilizing the IEEE 9-bus test system. For ease of analysis, we construct uncertainty sets by setting the RES forecast errors as ±65%, ±55%, ±45%, ±35%, and ±25%. Subsequently, we calculate the corresponding BC-OR and CH-EOR without ESS in operation (BC-OR 1 and CH-EOR 1) and with ESS in operation (BC-OR 2 and CH-EOR 2). We randomly generate 500 scenarios for RES output within each uncertainty set and then compute the corresponding global OSSs and the OSSs within BC-OR and CH-EOR, respectively. After that, the optimal average operating costs and the average operating costs based on BC-OR and CH-OR are compared, as shown in Table V, with values of the ratio to the optimal average operating cost.

TABLE V
COMPARISON RESULTS OF AVERAGE OPERATING COSTS

RES forecast error (%)	Without ESS in operation					With ESS in operation				
	Optimal average operating cost ($)	BC-OR 1		CH-EOR 1		Optimal average operating cost ($)	BC-OR 2		CH-EOR 2	
		Average operating cost ($)	Ratio	Average operating cost ($)	Ratio		Average operating cost ($)	Ratio	Average operating cost ($)	Ratio
±65	61008	67681	1.1094	61008	1.0000	59460	65469	1.1011	59460	1.0000
±55	60816	65839	1.0826	60816	1.0000	59374	63529	1.0700	59374	1.0000
±45	60660	64168	1.0578	60660	1.0000	59307	61828	1.0425	59307	1.0000
±35	60539	62818	1.0377	60539	1.0000	59256	60569	1.0222	59256	1.0000
±25	60452	61747	1.0214	60452	1.0000	59219	59645	1.0072	59219	1.0000

The simulation results demonstrate that the average operating cost based on the CH-EOR aligns with the optimal average operating cost, encompassing all corresponding OSSs. In contrast, the BC-OR is derived from a two-stage robust optimization method [32], aiming to find the optimal solution under the worst-case scenario and exhibiting a conservative bias. Consequently, as indicated in Table V, the average operating cost derived from the BC-OR surpasses the optimal average operating cost. This discrepancy grows with the increasing RES forecast errors, indicating that certain OSSs are excluded from the BC-OR. Notably, CH-EOR 2 outperforms CH-EOR 1. Thus, we can infer that CH-EOR offers superior economic outcomes compared with BC-OR, and the ESS contributes to a reduction in the operating costs of power grid.

D. Computational Efficiency Analysis

This subsection analyzes the computational efficiency of the proposed big-M preprocessing method for each test system. We set $m_1 = 1.5$, $m_2 = 10$, and $m_3 = 10^5$ for the big-M preprocessing method and set $M = 10^5$ for the traditional big-M method. The experiments are performed on the IEEE 9-bus, IEEE 30-bus, IEEE 57-bus, and IEEE 118-bus test systems, with or without ESS in operation. The RES forecast error is all assumed to be ±65%. Table VI shows the average computational time of generating one extending point in each simulation.

TABLE VI
COMPARISON OF AVERAGE COMPUTATIONAL TIME

Test system	Big-M method	Average computational time (s)	
		Without ESS in operation	With ESS in operation
IEEE 9-bus	Proposed	0.08	0.24
	Traditional	13.42	>1200.00
IEEE 30-bus	Proposed	0.13	0.72
	Traditional	2.62	248.39
IEEE 57-bus	Proposed	1.33	79.72
	Traditional	23.61	>1200.00
IEEE 118-bus	Proposed	1.80	2.06
	Traditional	>1200.00	>1200.00

According to Table VI, the computation is more efficient after applying the proposed big-M preprocessing method. When the ESS is in operation, the average computational time becomes longer due to the introduction of ESS operating constraints. Further, we can observe that the average computational time in the IEEE 9-bus test system is longer than that in the IEEE 30-bus test system based on the traditional big-M method. After applying the big-M preprocessing method, the average computational time in the IEEE 57-bus test system can also be longer than that in the IEEE 118-bus test system when the ESS is in operation. In general, the average computational time tends to increase with the expansion of the system scale, but sometimes smaller-scale systems require longer computational time. This is because the computational efficiency of mixed-integer programming is affected by many factors such as the solving scale, branching method, and node relaxation.

Usually, choosing an overlarge M value for the traditional big-M method will lead to worse node relaxation and significantly prolonged computational time. However, if the M value is set too small, it may result in calculational infeasibility. Thus, it is usually difficult to determine a suitable M for the traditional big-M method. In comparison, it is easier to determine m_1, m_2, and m_3 for the proposed big-M preprocessing method, which can further decrease the node relaxation during the branching process, resulting in fewer nodes to be examined. Thus, according to Table VI, the proposed big-M preprocessing method can significantly improve the computational efficiency of the proposed algorithm (averagely improved over 17 times).

It is worth mentioning that although the proposed big-M preprocessing method can significantly improve the efficiency of generating CH-EOR, the required computational time will also increase as the system scale increases. Additionally, when the number of DGs increases, the amount of vertices in the CH-EOR that need to be calculated will also increase. Therefore, further improvements to the proposed algorithm are still needed for larger-scale systems. In the future, we will further explore the decomposing and parallel-solving structure and dimensionality reduction methods for the CH-EOR.

V. CONCLUSION

This paper innovatively introduces the mathematical definition and geometric properties of the CH-EOR for power grids. We perform simulations on four modified test systems based on the proposed algorithms for generating the CH-EOR and the proposed big-M preprocessing method. The testing results reveal that the CH-EOR is significantly smaller (ranging from 0.02% to 11.79% of the GAR) and more economically efficient (with a 0.72% to 10.94% increase compared with the BC-OR). The proposed big-M preprocessing method enhances computational efficiency by an average of over 17 times compared with the traditional big-M method.

Future research will extend to the calculation of the CH-EOR based on AC optimal power flow (OPF), incorporating unit commitment, exploring the effect of different uncertainty sets on the CH-EOR, and developing algorithms for the rapid selection of OSSs from the CH-EOR for real-time scheduling.

APPENDIX A

A. Proof of Proposition 1

Proof The proof process mainly consists of three steps. Firstly, based on the uncertainty set $\varUpsilon_W$ of wind power output and the KKT conditions of the optimal operating point of the power grid, we demonstrate that $\varPsi$ is a union of a finite number of bounded polytopes by exhaustively enumerating the zero value of $\boldsymbol{\lambda}_j$ in the bilinear constraints. Then, based on the definition of convex combination, we prove that the convex hull $\varPsi^{conv}$ of $\varPsi$ is a bounded polytope. Lastly, by explaining that the CH-EOR $\varPsi_t^{conv}$ of each time period is a lower-dimensional subspace of $\varPsi^{conv}$, we further demonstrate that $\varPsi_t^{conv}$ is also a bounded polytope. The detailed process is as follows.

Firstly, since the uncertainty set $\varUpsilon_W$ is a bounded polytope, $\varUpsilon_W$ can be expressed by linear inequalities as $\varUpsilon_W=\{\boldsymbol{p}_W|\boldsymbol{J}\boldsymbol{p}_W+\boldsymbol{K}\le\boldsymbol{0}\}$, where matrix $\boldsymbol{J}$ and vector $\boldsymbol{K}$ represent the coefficients. According to constraint (1b), $\boldsymbol{p}_{G,t}$ is always bounded. Let $\varPsi_{\alpha,\beta}=\{\boldsymbol{p}_G|\boldsymbol{J}\boldsymbol{p}_W+\boldsymbol{K}\le\boldsymbol{0},\boldsymbol{E}_{1i}\boldsymbol{p}_G+\boldsymbol{F}_{1i}\boldsymbol{p}_W+\boldsymbol{G}_{1i}\boldsymbol{X}+\boldsymbol{H}_{1i}=\boldsymbol{0},\forall i\in\varOmega_\beta^{C_{q_1}^\alpha},\forall j\in\varOmega_{q_1}\backslash\varOmega_\beta^{C_{q_1}^\alpha}$, (3a), (3b), (3c)$\}$, where $\varOmega_{q_1}$ is the index set of q_1 equations; and $\varOmega_\beta^{C_{q_1}^\alpha}$ denotes the β^{th} α-combination from $\varOmega_{q_1},\alpha=0,1,\dots,q_1,\beta=1,2,\dots,C_{q_1}^\alpha$. Clearly, $\varPsi_{\alpha,\beta}$ is either empty or a bounded polytope with finite vertices, $\forall\alpha,\forall\beta$. Thus, $\varPsi=\bigcup\limits_{\forall\alpha,\forall\beta}\varPsi_{\alpha,\beta}$, i.e., $\varPsi$ is the union of finite bounded polytopes.

Then, let $V_{\alpha,\beta}$ denote the set of vertices of $\varPsi_{\alpha,\beta}$ and $\boldsymbol{v}_{\alpha,\beta}^i$ be the i^{th} vertex in $V_{\alpha,\beta}$. $\varPsi^{conv}$ is the convex hull of the finite vertices $\bigcup\limits_{\forall\alpha,\forall\beta}V_{\alpha,\beta}$. Clearly, the convex set that covers $\varPsi$ cannot be smaller than $\varPsi^{conv}$. Any point $v_{\alpha,\beta}\in\varPsi_{\alpha,\beta}$ can be denoted by the convex combination of $\boldsymbol{v}_{\alpha,\beta}^i\in V_{\alpha,\beta}$, i.e., $\boldsymbol{v}_{\alpha,\beta}=\sum\limits_i\rho_{\alpha,\beta}^i\boldsymbol{v}_{\alpha,\beta}^i$, where $\sum\limits_i\rho_{\alpha,\beta}^i=1,\rho_{\alpha,\beta}^i\ge0$. Further, $\boldsymbol{v}_{\alpha,\beta}^i$ can be represented by the convex combination of $v_j^{conv}\in V^{conv}$, i.e., $\boldsymbol{v}_{\alpha,\beta}^i=\sum\limits_j\mu_j^i\boldsymbol{v}_j^{conv}$, where $\sum\limits_j\mu_j^i=1,\mu_j^i\ge0$, and $\boldsymbol{v}_j^{conv}$ represents the j^{th} vertex in V^{conv}. Thus, $\boldsymbol{v}_{\alpha,\beta}=\sum\limits_i\rho_{\alpha,\beta}^i\sum\limits_j\mu_j^i\boldsymbol{v}_j^{conv}=\sum\limits_j\kappa_j^i\boldsymbol{v}_j^{conv}$, where $\kappa_j=\sum\limits_i\rho_{\alpha,\beta}^i\mu_j^i$, $\kappa_j\ge0$. Since $\sum\limits_j\kappa_j^i=\sum\limits_j\sum\limits_i\rho_{\alpha,\beta}^i\mu_j^i=\sum\limits_i\rho_{\alpha,\beta}^i\sum\limits_j\mu_j^i=1$, then $\varPsi_{\alpha,\beta}\in\varPsi^{conv}$, $\forall\alpha,\forall\beta$, i.e., $\varPsi\in\varPsi^{conv}$. Thus, $\varPsi^{conv}$ is the convex hull of $\varPsi$, which is a bounded polytope.

Lastly, $\varPsi_t^{conv}=\text{Pr}_{\boldsymbol{p}_{G,t}^{dim}}(\varPsi^{conv})$, i.e., the projection of $\varPsi^{conv}$ onto $\boldsymbol{p}_{G,t}^{dim}$-subspace, so $\varPsi_t^{conv}$ is a bounded polytope too [4], [42].

B. Proof of Proposition 2

Proof We propose to prove Proposition 2 by contradiction. Firstly, assume that the extending point obtained based on the optimization model (11) is not the extreme point of CH-EOR. Then, in the neighborhood of this extending point, we find a counterexample to prove that this extending point is not the optimal solution of (11). The detailed proof process is as follows.

Assuming the generated extending point $\boldsymbol{p}_{G,t}^{dim}$ is not the extreme point of $\varPsi_t^{conv}$, it could appear within/on the facet, or on the edge of $\varPsi_t^{conv}$, around which a sufficiently small neighborhood $\boldsymbol{\rho}$ must exist and contains no extreme points. According to Algorithm 1 and the quickhull algorithm [44] (neglecting the computation error resulting from the small initial convex hulls), the generated extending point is above $\{cf_{\gamma,t}^k, df_t^k\}$. Thus, $(\boldsymbol{cf}_t^k)^{\mathrm{T}}\boldsymbol{p}_{G,t}^{dim}+df_t^k>0$, and the distance from $\boldsymbol{p}_{G,t}^{dim}$ to facet $\{cf_{\gamma,t}^k, df_t^k\}$ is $d_0=\left|(\boldsymbol{cf}_t^k)^{\mathrm{T}}\boldsymbol{p}_{G,t}^{dim}+df_t^k\right|/\|\boldsymbol{cf}_t^k\|>0$.

If $\boldsymbol{p}_{G,t}^{dim}$ is on the edge (whose direction vector is $\boldsymbol{v}$) of Ψ_t^{conv}, then there must exist two points, i. e., $\boldsymbol{p}_1=(\boldsymbol{p}_{G,t}^{dim}+\tau\boldsymbol{v})\in\rho$ and $\boldsymbol{p}_2=(\boldsymbol{p}_{G,t}^{dim}-\tau\boldsymbol{v})\in\rho$, where $\tau\geq 0$ is a small enough positive coefficient. The distances from $\boldsymbol{p}_1$ and $\boldsymbol{p}_2$ to facet $\{cf_{\gamma,t}^k, df_t^k\}$ are $d_1=\left|(\boldsymbol{cf}_t^k)^{\mathrm{T}}(\boldsymbol{p}_{G,t}^{dim}+\tau\boldsymbol{v})+df_t^k\right|/\|\boldsymbol{cf}_t^k\|$ and $d_2=\left|(\boldsymbol{cf}_t^k)^{\mathrm{T}}(\boldsymbol{p}_{G,t}^{dim}-\tau\boldsymbol{v})+df_t^k\right|/\|\boldsymbol{cf}_t^k\|$, respectively. Since vector $\boldsymbol{cf}_t^k$ is not orthogonal to any facet of Ψ_t^{conv}, $(\boldsymbol{cf}_t^k)^{\mathrm{T}}\boldsymbol{v}\neq 0$. If $(\boldsymbol{cf}_t^k)^{\mathrm{T}}\boldsymbol{v}>0$, $d_1=d_0+\tau(\boldsymbol{cf}_t^k)^{\mathrm{T}}\boldsymbol{v}/\|\boldsymbol{cf}_t^k\|>d_0$, else $d_2=d_0+\tau\left(\boldsymbol{cf}_t^k\right)^{\mathrm{T}}\boldsymbol{v}/\|\boldsymbol{cf}_t^k\|>d_0$. Therefore, $\boldsymbol{p}_{G,t}^{dim}$ is not the farthest point above $\{cf_{\gamma,t}^k, df_t^k\}$, which does not agree with the optimization problem (11). If $\boldsymbol{p}_{G,t}^{dim}$ is within or on the facet of Ψ_t^{conv}, we can also find a direction vector $\boldsymbol{v}$ that is not orthogonal to vector $\{cf_{\gamma,t}^k\}$ and prove the contradiction similarly. Thus, the extending point generated based on $\{cf_{\gamma,t}^k, df_t^k\}$ is the extreme point of Ψ_t^{conv}.

C. Factors of RES and Load

As shown in Table AI, the factors for RES represent the output coefficients of RES 1 and RES 2, and multiplying them by the base power of RES 1 and RES 2 yields their actual output sequences, respectively. The factors of load represent the load level coefficients, and multiplying them by the base load results in the actual load level sequence.

TABLE AI
FACTORS OF RESS AND LOAD

Time step	Factor			Time step	Factor		
	RES 1	RES 2	Load		RES 1	RES 2	Load
1	1.0000	0.5761	0.9918	13	0.8696	1.0020	1.2932
2	1.2500	0.6343	0.8796	14	1.2510	0.7062	1.3236
3	1.1413	0.3822	0.8582	15	1.2174	0.5281	1.3535
4	0.7609	0.7060	0.8283	16	1.3043	0.6401	1.3834
5	0.8696	1.1763	0.8710	17	1.1957	0.5526	1.3336
6	1.0870	1.2363	0.8652	18	1.3033	0.8088	1.3246
7	0.5652	1.3240	0.8796	19	1.5217	0.6780	1.3136
8	0.7826	1.3542	0.8818	20	1.7391	0.5161	1.2031
9	1.3587	1.3384	0.9117	21	1.3143	0.8580	1.1932
10	1.3043	1.3246	0.9824	22	1.0887	0.5442	1.1881
11	1.4130	1.2641	1.0826	23	1.7391	0.7161	0.9023
12	1.0870	1.1201	1.2031	24	1.5217	0.6460	0.8918

REFERENCES

[1] I. Kougias, N. Taylor, G. Kakoulaki *et al.*, "The role of photovoltaics for the european green deal and the recovery plan," *Renewable and Sustainable Energy Reviews*, vol. 144, p. 111017, Jul. 2021.

[2] B. Room. (2021, Jan.). Executive order on tackling the climate crisis at home and abroad. [Online]. Available: https://www.federalregister.gov/documents/2021/02/01/2021-02177/tackling-the-climate-crisis-at-home-and-abroad

[3] J. Xi. (2020, Sept.). Statement at the general debate of the 75th session of the united nations general assembly. [Online]. Available: http://english.scio.gov.cn/topnews/2020-09/23/content_76731466.htm

[4] W. Wei, F. Liu, and S. Mei, "Dispatchable region of the variable wind generation," *IEEE Transactions on Power Systems*, vol. 30, no. 5, pp. 2755-2765, Sept. 2015.

[5] B. Hu and L. Wu, "Robust SCUC considering continuous/discrete uncertainties and quick-start units: a two-stage robust optimization with mixed-integer recourse," *IEEE Transactions on Power Systems*, vol. 31, no. 2, pp. 1407-1419, Mar. 2016.

[6] H. Haghighat and B. Zeng, "Stochastic and chance-constrained conic distribution system expansion planning using bilinear benders decomposition," *IEEE Transactions on Power Systems*, vol. 33, no. 3, pp. 2696-2705, May 2018.

[7] P. Li, D. Yu, M. Yang *et al.*, "Flexible look-ahead dispatch realized by robust optimization considering CVaR of wind power," *IEEE Transactions on Power Systems*, vol. 33, no. 5, pp. 5330-5340, Sept. 2018.

[8] X. Lu, K. W. Chan, S. Xia *et al.*, "Security-constrained multiperiod economic dispatch with renewable energy utilizing distributionally robust optimization," *IEEE Transactions on Sustainable Energy*, vol. 10, no. 2, pp. 768-779, Apr. 2019.

[9] Y. Shi, S. Dong, C. Guo *et al.*, "Enhancing the flexibility of storage integrated power system by multi-stage robust dispatch," *IEEE Transactions on Power Systems*, vol. 36, no. 3, pp. 2314-2322, May 2021.

[10] Z. Chen, Z. Li, C. Guo *et al.*, "Fully distributed robust reserve scheduling for coupled transmission and distribution systems," *IEEE Transactions on Power Systems*, vol. 36, no. 1, pp. 169-182, Jan. 2021.

[11] Z. Chen, S. Dong, C. Guo *et al.*, "Fully distributed risk-based robust reserve scheduling for bulk hybrid AC-DC systems," *CSEE Journal of Power and Energy Systems*, vol. 9, no. 2, pp. 634-644, Mar. 2023.

[12] M. Ebrahimi and A. Sheikhi, "A local integrated electricity-heat market design among multi smart energy hubs with renewable energy generation uncertainty," *Electric Power Systems Research*, vol. 218, p. 109217, May 2023.

[13] S. Chen, Z. Wei, G. Sun *et al.*, "Convex hull based robust security region for electricity-gas integrated energy systems," *IEEE Transactions on Power Systems*, vol. 34, no. 3, pp. 1740-1748, May 2019.

[14] J. Xiao, G. Zu, Y. Wang *et al.*, "Model and observation of dispatchable region for flexible distribution network," *Applied Energy*, vol. 261, p. 114425, Mar. 2020.

[15] J. Xiao, W. Gu, C. Wang *et al.*, "Distribution system security region: definition, model and security assessment," *IET Generation, Transmission & Distribution*, vol. 6, no. 10, pp. 1029-1035, Oct. 2012.

[16] J. Xiao, G. Zu, X. Gong *et al.*, "Model and topological characteristics of power distribution system security region," *Journal of Applied Mathematics*, vol. 2014, p. 327078, Jul. 2014.

[17] J. Xiao, G. Zu, X. Gong *et al.*, "Observation of security region boundary for smart distribution grid," *IEEE Transactions on Smart Grid*, vol. 8, no. 4, pp. 1731-1738, Jul. 2017.

[18] G. Zu, J. Xiao, and K. Sun, "Mathematical base and deduction of security region for distribution systems with DER," *IEEE Transactions on Smart Grid*, vol. 10, no. 3, pp. 2892-2903, May 2019.

[19] C. Wan, J. Lin, W. Guo *et al.*, "Maximum uncertainty boundary of volatile distributed generation in active distribution network," *IEEE Transactions on Smart Grid*, vol. 9, no. 4, pp. 2930-2942, Jul. 2018.

[20] J. Zhao, T. Zheng, and E. Litvinov, "Variable resource dispatch through do-not-exceed limit," *IEEE Transactions on Power Systems*, vol. 30, no. 2, pp. 820-828, Mar. 2015.

[21] W. Wei, F. Liu, and S. Mei, "Real-time dispatchability of bulk power systems with volatile renewable generations," *IEEE Transactions on Sustainable Energy*, vol. 6, no. 3, pp. 738-747, Jul. 2015.

[22] H. D. Nguyen, K. Dvijotham, and K. Turitsyn, "Constructing convex inner approximations of steady-state security regions," *IEEE Transactions on Power Systems*, vol. 34, no. 1, pp. 257-267, Jan. 2019.

[23] Y. Liu, Z. Li, Q. H. Wu *et al.*, "Real-time dispatchable region of renewable generation constrained by reactive power and voltage profiles in ac power networks," *CSEE Journal of Power and Energy Systems*, vol. 6, no. 3, pp. 528-536, Sept. 2020.

[24] Y. Liu, Z. Li, W. Wei *et al.*, "Data-driven dispatchable regions with potentially active boundaries for renewable power generation: concept and construction," *IEEE Transactions on Sustainable Energy*, vol. 13, no. 2, pp. 882-891, Apr. 2022.

[25] H. Ma, R. Jiang, and Z. Yan, "Distributionally robust co-optimization of power dispatch and do-not-exceed limits," *IEEE Transactions on Power Systems*, vol. 35, no. 2, pp. 887-897, Mar. 2020.

[26] W. Lin, Z. Yang, J. Yu *et al.*, "Tie-line security region considering time coupling," *IEEE Transactions on Power Systems*, vol. 36, no. 2, pp. 1274-1284, Mar. 2021.

[27] T. Jiang, R. Zhang, X. Li *et al.*, "Integrated energy system security region: concepts, methods, and implementations," *Applied Energy*, vol. 283, p. 116124, Feb. 2021.

[28] J. Su, H. D. Chiang, and L. F. C. Alberto, "Two-time-scale approach

to characterize the steady-state security region for the electricity-gas integrated energy system," *IEEE Transactions on Power Systems*, vol. 36, no. 6, pp. 5863-5873, Nov. 2021.

[29] J. Su, H. D. Chiang, Y. Zeng *et al*., "Toward complete characterization of the steady-state security region for the electricity-gas integrated energy system," *IEEE Transactions on Smart Grid*, vol. 12, no. 4, pp. 3004-3015, Jul. 2021.

[30] T. Yang and Y. Yu, "Steady-state security region-based voltage/var optimization considering power injection uncertainties in distribution grids," *IEEE Transactions on Smart Grid*, vol. 10, no. 3, pp. 2904-2911, May 2019.

[31] C. Shao, X. Wang, M. Shahidehpour *et al*., "Power system economic dispatch considering steady-state secure region for wind power," *IEEE Transactions on Sustainable Energy*, vol. 8, no. 1, pp. 268-278, Jan. 2017.

[32] Y. Cho, T. Ishizaki, N. Ramdani *et al*., "Box-based temporal decomposition of multi-period economic dispatch for two-stage robust unit commitment," *IEEE Transactions on Power Systems*, vol. 34, no. 4, pp. 3109-3118, Jul. 2019.

[33] H. Xu, B. Jiang, B. Feng *et al*., "The concept of economic operating region and its convex hull solution method for quantifying the influence of grid uncertainty on scheduling plan," *Proceedings of the CSEE*, vol. 43, no. 16, pp. 6288-6299, Aug. 2023.

[34] H. Xu, B. Feng, C. Wang *et al*., "Exact box-constrained economic operating region for power grids considering renewable energy sources," *Journal of Modern Power Systems and Clean Energy*, vol. 12, no. 2, pp. 514-523, Mar. 2024.

[35] J. Guan, H. Tang, K. Wang *et al*., "A parallel multi-scenario learning method for near-real-time power dispatch optimization," *Energy*, vol. 202, p. 117708, Jul. 2020.

[36] J. Guan, H. Tang, J. Wang *et al*., "A gan-based fully model-free learning method for short-term scheduling of large power system," *IEEE Transactions on Power Systems*, vol. 37, no. 4, pp. 2655-2665, Jul. 2022.

[37] Y. Zhou, W. Lee, R. Diao *et al*., "Deep reinforcement learning based real-time AC optimal power flow considering uncertainties," *Journal of Modern Power Systems and Clean Energy*, vol. 10, no. 5, pp. 1098-1109, Sept. 2022.

[38] A. R. Sayed, C. Wang, H. I. Anis *et al*., "Feasibility constrained online calculation for real-time optimal power flow: a convex constrained deep reinforcement learning approach," *IEEE Transactions on Power Systems*, vol. 38, no. 6, pp. 5215-5227, Nov. 2023.

[39] Y. Zhao, Y. Chen, and W. Sun, "Region dispatch method and market trading strategy for multi-microgrid distribution system," *Power System Technology*, vol. 46, no. 1, pp. 47-56, Jan. 2022.

[40] P. Yang and A. Nehorai, "Joint optimization of hybrid energy storage and generation capacity with renewable energy," *IEEE Transactions on Smart Grid*, vol. 5, no. 4, pp. 1566-1574, Jul. 2014.

[41] Z. Tan, H. Zhong, Q. Xia *et al*., "Non-iterative multi-area coordinated dispatch via condensed system representation," *IEEE Transactions on Power Systems*, vol. 36, no. 2, pp. 1594-1604, Mar. 2021.

[42] S. Boyd and L. Vandenberghe, *Convex Optimization*. Cambridge: Cambridge University, 2004.

[43] Z. Tan, H. Zhong, Q. Xia *et al*., "Estimating the robust *p-q* capability of a technical virtual power plant under uncertainties," *IEEE Transactions on Power Systems*, vol. 35, no. 6, pp. 4285-4296, Nov. 2020.

[44] C. B. Barber, D. P. Dobkin, and H. Huhdanpaa, "The quickhull algorithm for convex hulls," *ACM Transactions on Mathematical Software*, vol. 22, no. 4, pp. 469-483, Dec. 1996.

[45] R. D. Zimmerman and C. E. Murillo-Sanchez. (2020, Dec.). MATPOWER (version 7.1). [Online]. Available: https://matpower.org

Huating Xu received the B.S. degree from Sichuan University, Chengdu, China, in 2012, and the M.S. degree from China Electric Power Research Institute, Beijing, China, in 2020. Now, he is working towards the Ph.D. degree with the College of Electrical Engineering, Zhejiang University, Hangzhou, China. He was an Electrical Engineer with the China General Nuclear Power Group, Dalian, China, from 2012 to 2017. His current research interests include deep reinforcement learning, reactive power and tie-line power adjustment, optimal power flow, and economic dispatching region.

Bin Feng received the B.S. degree in electrical engineering and its automation from the North Chine Electric Power University, Beijing China, in 2019. He is presently working towards the Ph.D. degree in Zhejiang University, Hangzhou, China. His current research interests include deep reinforcement learning, federated learning, energy management, and forecasting.

Gang Huang received the Ph.D. degree in electrical engineering from Zhejiang University, Hangzhou, China, in 2018. During 2015-2016, he was with Argonne National Laboratory, Argonne, USA. Presently, he is an Assistant Professor with the College of Electrical Engineering, Zhejiang University. Prior to this role, he served as a Senior Researcher at Zhejiang Lab, Hangzhou, China. His primary research interests include artificial intelligence for power and energy systems.

Mingyang Sun received the Ph.D. degree from the Department of Electrical and Electronic Engineering, Imperial College London, London, U. K., in 2017. From 2017 to 2019, he was a Research Associate and a DSI Affiliate Fellow with Imperial College London. He is currently a Professor with Zhejiang University, Hangzhou, China. He is also an Honorary Lecturer with Imperial College London. His research interests include artificial intelligence in energy systems and cyber-physical energy system security and control.

Houbo Xiong received the B.Sc. degree from the College of Electrical Engineering, Hubei University of Technology, Wuhan, China, in 2021. He is currently working toward the Ph.D. degree with the College of Electrical Engineering, Zhejiang University, Hangzhou, China. His research interests include optimal operation of power systems, renewable energy integration, and integrated energy systems.

Chuangxin Guo received the Ph. D. degree in electrical engineering from Huazhong University of Science and Technology, Wuhan, China, in 1997. He is currently a Professor with the College of Electrical Engineering, Zhejiang University, Hangzhou, China. His research interests include power system operation and planning, and power systems information and communication technologies.